INSTABILITIES ON HIGH TEMPERATURE ISOTHERMAL CREEP PERFORMANCE IN Ni-BASED SINGLE CRYSTAL SUPERALLOYS

A Thesis

by

SEUNGJUN LEE

Submitted to the Office of Graduate and Professional Studies of
Texas A&M University
in partial fulfillment of the requirements for the degree of

MASTER OF SCIENCE

Chair of Committee,	Jean-Briac le Graverend
Committee Members,	Amine Benzerga
	Ibrahim Karaman
Head of Department,	Rodney Bowersox

August 2019

Major Subject: Aerospace Engineering

ABSTRACT

Nickel-based singe crystal superalloys are a class of metallic materials with a combination of high-temperature strength, toughness, and resistance to degradation in oxidizing environments, which makes them great candidates for aircraft engine turbine blades that operate at temperatures beyond 1000℃. The lifetime of such materials is directly connected to the integrity of the strengthening phase, or the so-called the γ' precipitates. Uniaxial thermo-mechanical environments have already been shown to lead to the phase transformations, microstructure gradients, and lattice rotation, which all contribute to the change in mechanical properties. Stress field in turbine blades are, however, multiaxial, and the load bearing section of the turbine blades decreases due to depletion of the γ' precipitates during oxidation. In order to accurately predict the lifetime of the turbine blades, it is critical to understand how multiaxiality and oxidation kinetics affect the damage evolution during creep. Samples of the second-generation Ni-based single crystal superalloy, René N5, were prepared with specified triaxialities using notches according to Bridgman's equation for creep tests. Through SEM analysis, it was found that the material had too much γ/γ′ eutectics that were not properly eliminated during the heat treatment, which resulted in earlier fractures. Kachanov-Rabotnov creep-damage model with Hayhurst stress criterion was modified to account for the depletion of the strengthening phase due to oxidation. Among many factors that affect the kinetics of oxidation, the effects of surface roughness and the initial plastic strain were studied. According to a number of studies, it was found that the kinetics of oxidation tends to increase with decrease in the surface roughness and increase in initial plastic

strain. A dimensionless variable e_{ox} was introduced to represent the depleted zone thickness and its evolution was simulated varying the two aforementioned factors. Simulation results of creep curves both in vacuum and in air were analyzed, and the results showed conceptually matching trends found in the literatures.

ACKNOWLEDGEMENTS

I would like to thank my advisor, Dr. le Graverend for his continuous guidance and support throughout the course of this research.

Thanks also go to my friends and colleagues and the department faculty and staff for making my time at Texas A&M University a great experience.

Finally, thanks to my mother and father for their encouragement and to my girlfriend for her patience and love.

CONTRIBUTORS AND FUNDING SOURCES

Contributors

This work was supervised by the committee chair Dr. le Graverend from the Department of Aerospace Engineering.

The material for creep tests, René N5, was provided by General Electric, and the SEM analysis was performed at Material Characterization Facility at Texas A&M University.

The simulations were performed using the computing resources from Laboratory for Molecular Simulation (LMS) and High Performance Research Computing (HPRC) at Texas A&M University.

Funding Sources

This work was also made possible in part by the Air Force under Grant Number FA9550-17-1-0233. Its contents are solely the responsibility of the authors and do not necessarily represent the official views of the AFOSR.

NOMENCLATURE

$\underline{\underline{\sigma_{eff}}}$	effective stress tensor
$\underline{\underline{m^s}}$	orientation tensor
$\underline{n^s}$	normal to the slip system planes
$\underline{l^s}$	slip direction in the slip planes
γ^s	viscoplastic shear on the slip system *s*
$\underline{\underline{\varepsilon_p}}$	viscoplastic strain tensor
$\underline{\underline{\sigma}}$	applied stress tensor
p	accumulated viscoplastic strain
f_{eq}	volume fraction of the γ' phase at thermodynamic equilibrium
f_s	small γ' precipitates volume fraction
f_l	large γ' precipitates volume fraction
$\dot{T}$	heating/cooling rate
τ^s	resolved shear stress on the slip system *s*
r^s	isotropic hardening on the slip system *s*
τ_0^s	critical resolved shear stress on the slip system *s*
h_{sj}	components of the hardening matrix
ρ^s	isotropic state variable on the slip system *s*
Q	dislocation hardening
τ_{Orowan}	Orowan stress

w_{001}	γ channel width along the [001] direction
G	shear modulus
B	Burgers vector magnitude
$f_{thermal}$	contribution of the thermal loading leading to w_{001} evolution
$f_{mechanic}$	contribution of the mechanical loading leading to w_{001} evolution
$f_{isotropic}$	contribution of the thermal holding leading to w_{001} evolution
$f_{diffusion}$	contribution of the diffusion process leading to w_{001} evolution
$\tau_{diffusion}$	characteristic time of diffusion
ξ	strain rate sensitivity of the γ′ rafting
x^s	kinematic hardening on the slip system *s*
α^s	kinematic variable on the slip system *s*
a^*	temperature dependent recovery variable
D_c	damage scalar
$\Delta\varepsilon_p$	plastic strain amplitude
$\Delta\,\sigma$	stress amplitude
e_{ox}	non-dimensional depleted zone

TABLE OF CONTENTS

Page

LIST OF FIGURES

Page

LIST OF TABLES

Page

1. INTRODUCTION

1.1. Microstructure of Ni-based Single Crystal Superalloys

The advantage of single crystal superalloys is that there are no grain boundaries, which gives superior creep and thermal fatigue resistance compared to polycrystalline alloys as the grain boundaries are preferred places for damage and pore nucleations at high-temperature/low stress [1]. Single crystal superalloys also have an increased incipient melting temperature because of the absence of secondary alloying elements such as B and Zr that are commonly employed for grain boundary strengthening in case of wrought Ni-based alloys [1]. The microstructure of these alloys is a dual phase that consists of the long-range $L1_2$ ordered γ' precipitates and γ matrix. In <001>-oriented Ni-based single crystal superalloys, the γ' precipitates appear as cubes all aligned in <001> directions, which leaves the γ phase in narrow and parallel channels between the γ' precipitates. These two phases show perfectly coherent interfaces [2, 3]. The $L1_2$ ordered γ' phase has a stoichiometry of the structure is A_3B, typically Ni_3Al in case of Ni-based single crystal superalloys. The γ' phase directionally coarsens into platelets during high temperature/low stress testing [4, 5] (see Figure 1), known as rafting, which causes difficulties for dislocations to move along the loading direction when tension is applied along the crystallographic orientation of the alloys, <001>. The high thermo-mechanical resistance is in fact directly related to the size and the volume fraction of the γ' precipitates, and it is commonly known that the optimum creep resistance is achieved when the mean cube edge

of the γ' precipitates is approximately 0.45 μm and the volume fraction is close to 70% at temperatures up to 950°C [6].

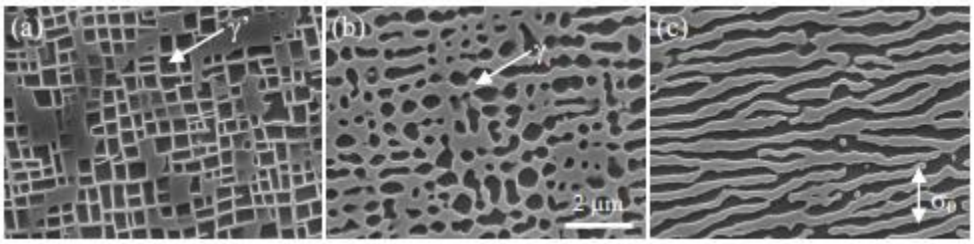

Figure 1. γ' rafting during a creep test of a <001> oriented MC2 at 1050°C /160MPa: γ/γ' microstructure at the beginning of the experiment (a), during primary creep stage (b), and during secondary creep stage (c)
Reprinted from [7].

1.2. Creep

With the increase of Turbine Entry Temperature (TET) and the efficiency of the engines, it becomes critical to understand the superalloy' resistance to creep, or more specifically, the microstructural evolution and damage mechanisms at high temperature and low stress. Creep is generally described by three different stages: primary, secondary, and tertiary, and there is an initial incubation period before the primary stage [5]. At the initial incubation period during the creep test at high temperature and low stress, dislocations percolate through the γ channel, and the γ' precipitates delay this process, which results into dislocations cross-slipping and bowing through the γ matrix channels. When the dislocations spread enough to a point where macroscopic strains can be measured, primary creep stage begins.

During the primary stage, dislocations continue to propagate in the γ channels and accumulate at the interface between γ and γ' phases, forming a dislocation network that

protects γ' precipitates from being sheared by dislocations. This leads to a decrease in the strain rate over time, and eventually reaches the minimum strain rate, or beginning of the secondary creep. Directional coarsening, or rafting, of the γ' precipitates is influenced by the misfit stress that is due to the difference between the lattice parameters between the γ and γ' phases. The γ' precipitates coalesce along the vertical channels which are in compression in case of negative lattice misfit alloys in tension. This rafting process is shown in Figure 1. The minimum creep rate that was achieved at the end of the primary creep stage continues during the secondary creep stage during which dislocations only move in the horizontal γ channels. At the end of the secondary creep stage, the creep rate begins to increase with time, and the material goes into the tertiary creep regime. At this stage, the mobile dislocation density increases which results into a larger number of jogged segments that eventually increases the climb velocity, thus the creep rate [8].

Destabilization of the dislocation network at the γ/ γ' interface occurs which leads the dislocation to enter the γ' phase. This accelerates the creep rate and finally leads to the material failure during the tertiary creep stage. A multi-interrupted creep test of the first-generation Ni-based single crystal superalloy MC2 at 1050°C/160 MPa with corresponding SEM images that reveals the microstructural evolution is shown in Figure 2.

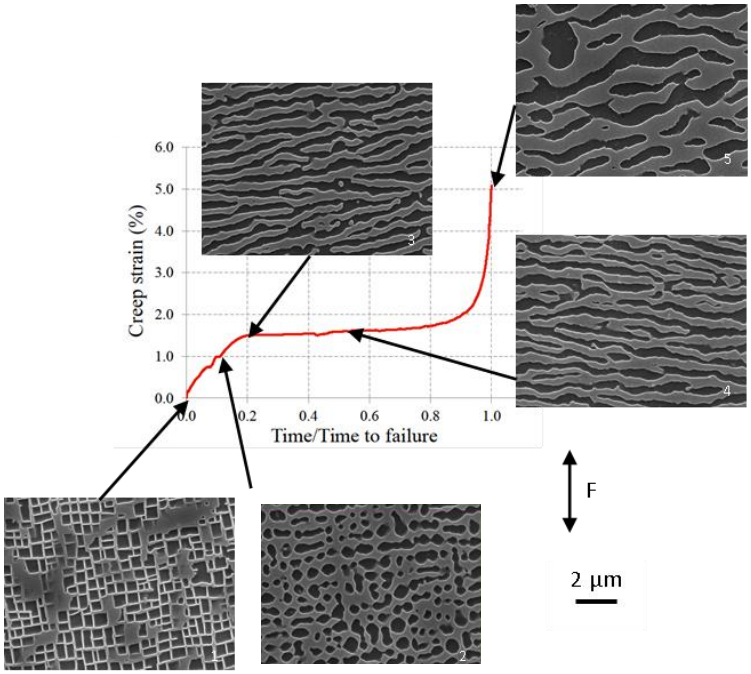

Figure 2. Microstructural evolutions during an isothermal creep test at 160 MPa/1050°C. 1) as received, 2) during primary stage, 3) and 4) secondary stage, 5) near fracture Reprinted from [7].

Based on several studies previously conducted on Ni-based single crystal superalloys, the creep behavior of such materials is known to be directly related to the integrity of the γ' precipitates, and many studies have showed that uniaxial thermo-mechanical environments lead to dissolution/precipitation of the γ' phase [9, 10], microstructure gradients [11], and lattice rotation [12, 13], which all contribute to the change in mechanical properties and lifetime. The stress state in turbine blades are, however, multiaxial and these turbine blades operate in oxidizing environments, which calls for additional investigations on damage due to multiaxiality and oxidation that may change kinetics of microstructural instabilities. Figure 3 shows a significant misorientation of the γ' rafts that are tilted up to 18° with respect to the macroscopic loading axis at the center of the specimen where the stress field has the highest multiaxial state due to the

asymmetric bi-notches [7]. In this figure, the EBSD analysis also indicates that there are multiple regions near the center of the specimen of which orientation is off the original crystallographic orientation [001]. This experiment was accompanied with a thermal jump from 1050°C to 1200°C for 30 seconds, which created tertiary (fine) γ' precipitates with a volume fraction depending on the accumulated plastic strain. That also contributed to the change in mechanical properties [14]. However, lattice rotation and tertiary precipitates will not be discussed in details as the proposed research focuses on damage due to multiaxiality and oxidation in isothermal conditions.

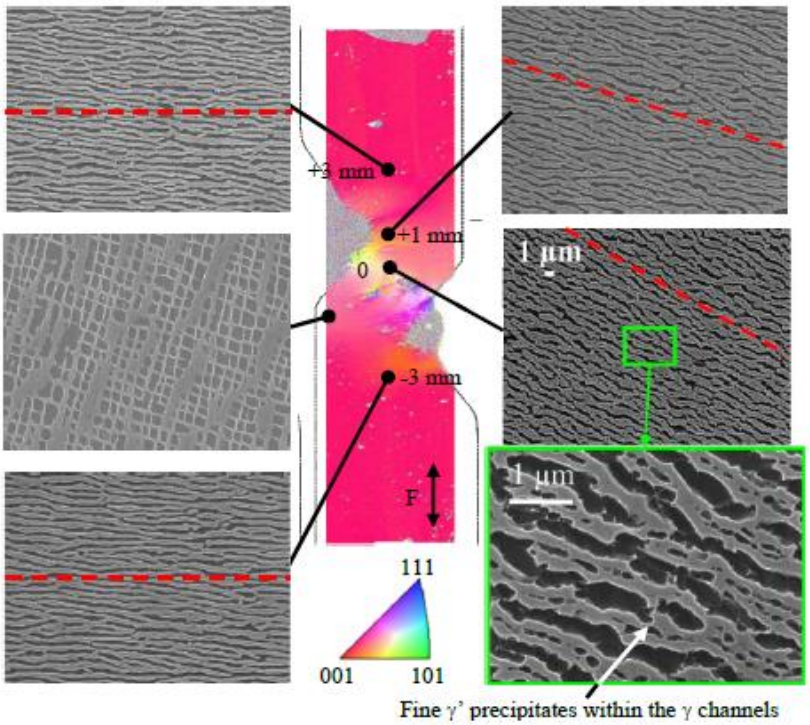

Figure 3. Longitudinal observations of the γ' rafted microstructure at the end of the test by SEM
Reprinted from [10].

1.3. Oxidation

When there are interactions between the environment and the superalloys, such as oxidation and/or corrosion, the mechanisms related to the oxide scale growth can affect the microstructural stability and, therefore, the mechanical behavior and lifetime [7, 15]. The fundamental reason on this phenomenon is the depletion process of the γ' precipitates during the formation of the oxide scale. As a reminder, the volume fraction of the γ' precipitates is what makes superalloys creep resistant. Depletion of the γ' precipitates is, therefore, equivalent to having a decrease in the load-bearing section. This increases the effective stress and eventually expedites the overall damage kinetics of the superalloys. The depletion process is well illustrated in Figure 4. During the oxidation, S becomes S′ due to the formation of the depleted zone of thickness e.

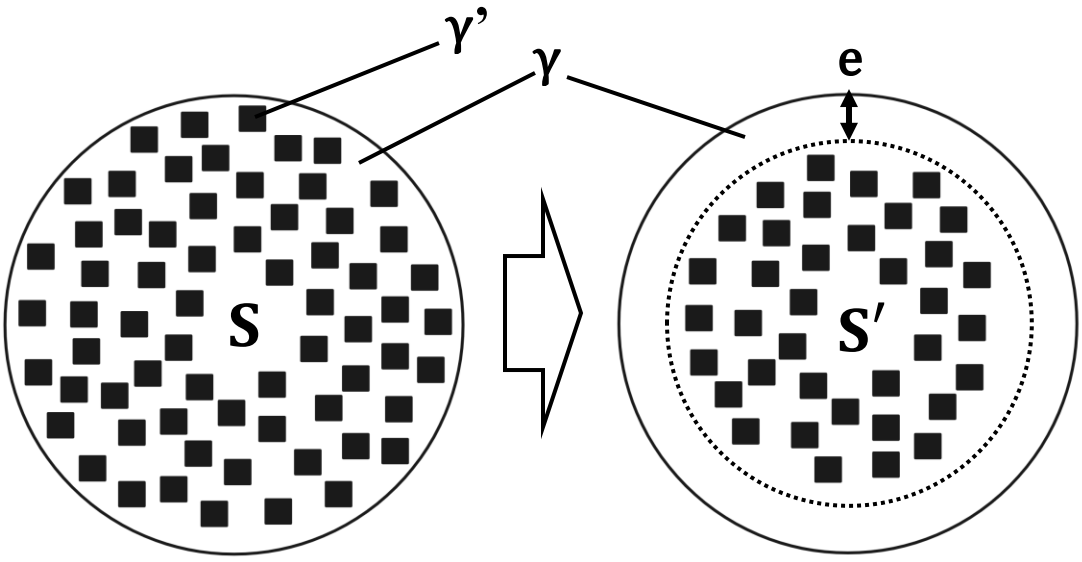

Figure 4. Depletion of the γ' precipitates during oxidation

1.3.1. Effect of surface roughness

Grinding the surface of the superalloys to a certain degree is a simple and easy way to prepare superalloys in order to control the oxidation kinetics [16]. In case of the second-generation Ni-based single crystal superalloys, DD6, it was found that the initial polishing of the samples has favored the growth of oxide scale. Pei, et al. explains that this phenomenon occurs because the types of oxide scales are different depending on the initial surface roughness. It is mainly the aluminum oxide, so called protective layer, that is formed when the surface is relatively rough, and other heavy oxides when the surface is relatively fine [17]. This is due to different segregational behaviors of alloying elements that result into dendrites during the solidification process of the superalloys. The interdendritic regions have high concentration of Al whereas the dendritic regions are rich Ni. When the surface is rough, it is mostly the interdendritic region that is exposed to the surface, which causes the formation of the protective layer that prevents further oxidation. When the surface is relatively fine, larger areas of the dendritic regions are exposed than that of interdendritic regions, which then causes the formation of NiO or Co_3O_2. This phenomenon was well observed in thermogravimetric tests of DD6 at 1000°C for 100 hours. In the test, each DD6 sample was prepared for different surface roughness, and it was observed that the samples with finer surface roughness showed higher oxidation kinetics [17].

However, it was interesting to observe that reducing the initial surface roughness to finer degree does not always result in higher growth of oxide scale. With Ra being the surface roughness, it showed higher oxidation scale growth for Ra = 91 nm than for Ra =

19 nm. This test result suggests that there may be a critical value of the initial surface roughness that will favor the oxidation the most. This phenomenon can be explained with the illustration shown in Figure 5. When the surface is prepared at the nanoscale, it is easier for oxygen molecules to react with the material when the surface is a little rough than the surface being completely flat.

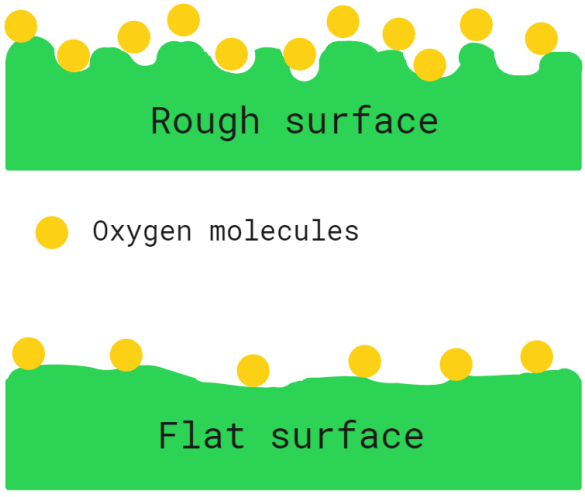

Figure 5. Illustration of oxygen chemisorption

1.3.2. Effect of plasticity

Initial plastic strain also affects the kinetics of oxidation. Diffusion process of chemical species at the interface between the alloy and the oxide scale is accelerated by pipe-line diffusion along dislocations or defects that are induced by plastic deformation [18]. The pipe line diffusion begins by the accumulation of foreign atoms that are preferably deposited in the area near the dislocation line. This accumulation is also called

as Cottrell atmosphere which is illustrated in Figure 6. Such phenomenon at which initial plastic strain favors the kinetics of oxidation was well observed in an experiment from Dubey, et al. where the kinetics of oxidation of carbon steel samples that were exposed in lithiated water increased with an increase in cold work percent [19]. The work from Reuchet, et al. also showed the same trend with MARM 509 that showed higher kinetics of oxidation with an increase in plastic strain amplitude during low cycle fatigue tests [18].

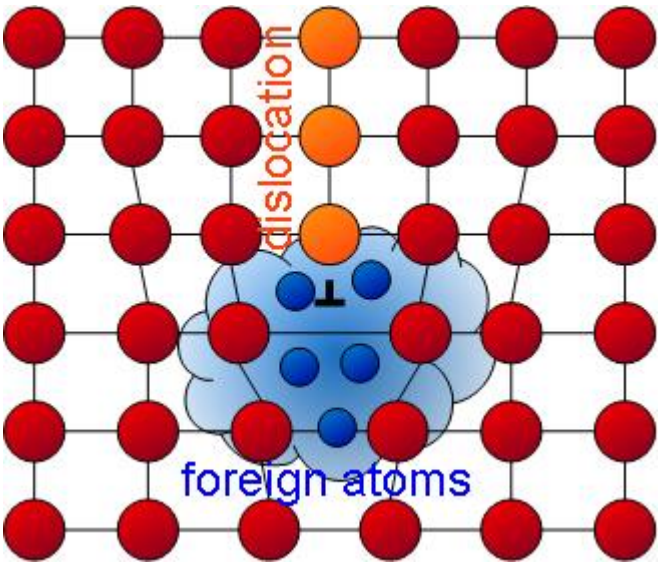

Figure 6. Cottrell atmosphere
Reprinted from [20].

2. SYSTEM SET-UP AND EXPERIMENTS

2.1. Creep Machine Design and Assembly

Figure 7 shows the system of equipment for creep tests that has been designed and assembled during the research. A furnace E4 chamber with an infrared 8 kW quad elliptical quarts lamp from Research Inc. (Figure 8 shows the illustration of the heating mechanism) was chosen for the experiment as it is capable of rapid heating, 275°C in 3 seconds. Cooling flow of 5T chiller from Skyline Industry was connected to the furnace in order to maintain a safe operational surrounding temperature.

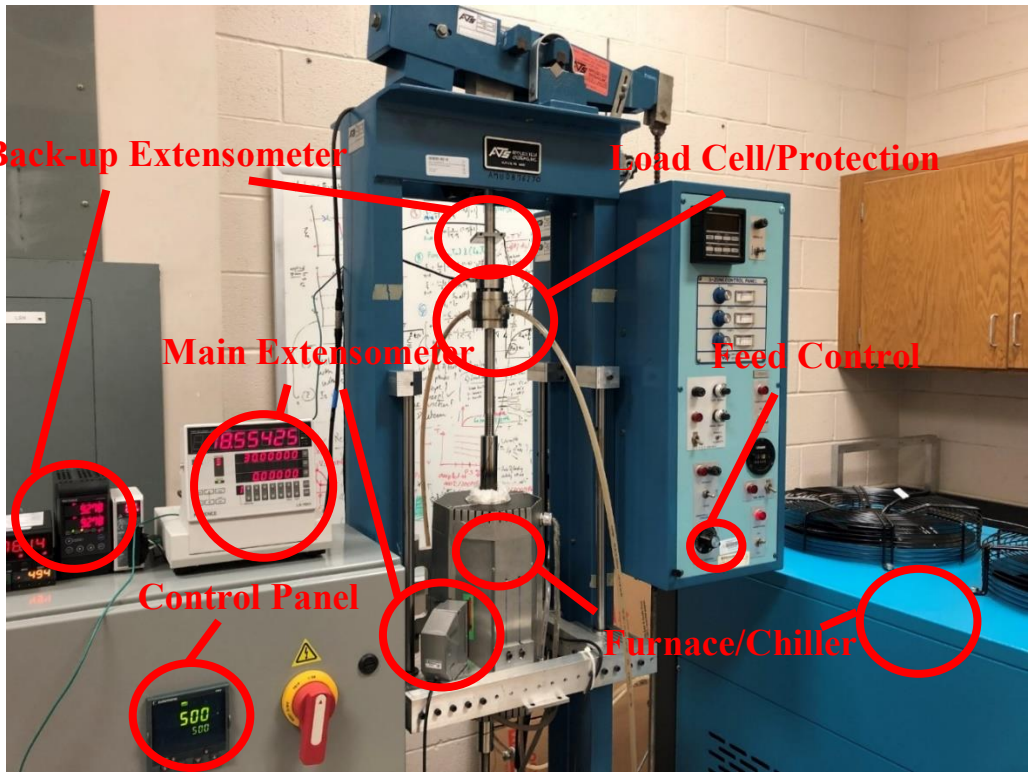

Figure 7. Complete assembly of the system designed for creep experiments

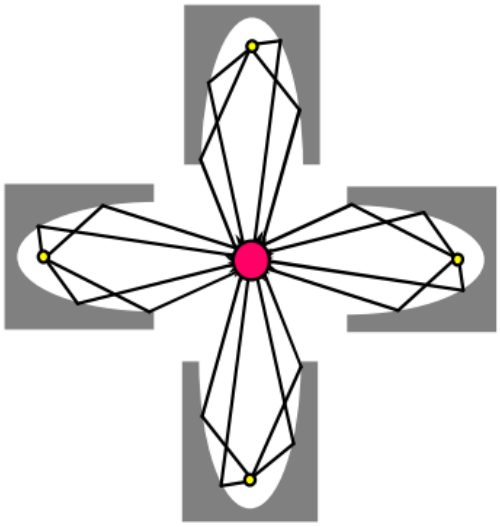

Figure 8. Illustration of eliptical reflectios and heating lamps
Reprinted from [21].

A laser micrometer LS-7000 from Keyence, which measures the distance between the two references without any contacts, was used to record the displacement of two metallic flags (Figure 9) that are positioned as close as possible on the specimen gauge area. It is also important to note that these extensometers are 6 mm off the main axis of the furnace because the laser could possibly be blocked by the sample and the distance between the flags cannot be measured. A 1-D laser displacement sensor LK-G5000 from Keyence was also positioned on top of the machine frame to measure the distance moved by the aluminum plate that is attached on top of the main axis. The measurements may not be as accurate as the ones made by the main extensometer, but this back up 1-D laser sensor can work as a redundant measuring system in case of a loss of flag positions of the main extensometers for any possible reasons, such as large radiation changes during non-isothermal loading.

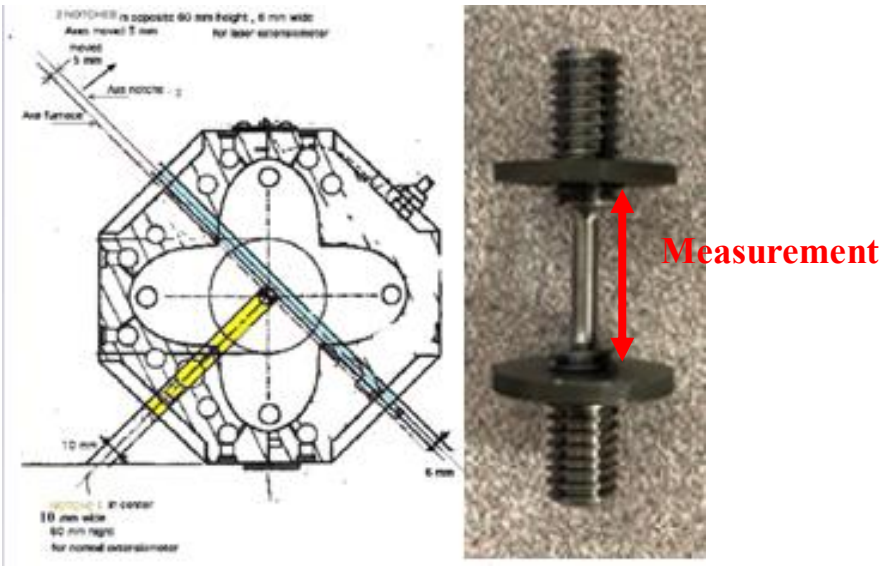

Figure 9. A) main extensometers position illustration B) a sample with flags Adapted from [21].

As the range of temperature for the proposed research is 900 °C to 1200 °C, it was critical to design and apply safety systems that can power off the furnace when the system encounters any errors in order to prevent any possible hazards. Three safety systems were designed using the mechanical relays. The contact switch shown in Figure 10 was installed at the lever arm and designed to be triggered when fracture occurs on the sample. Once the button is pushed, a normally closed relay that is wired into the emergency stop in the control panel opens, which then also opens the emergency stop circuit that will power off the furnace. This switch is to shut down the system when the sample has been broken and it is no longer needed for the furnace to operate.

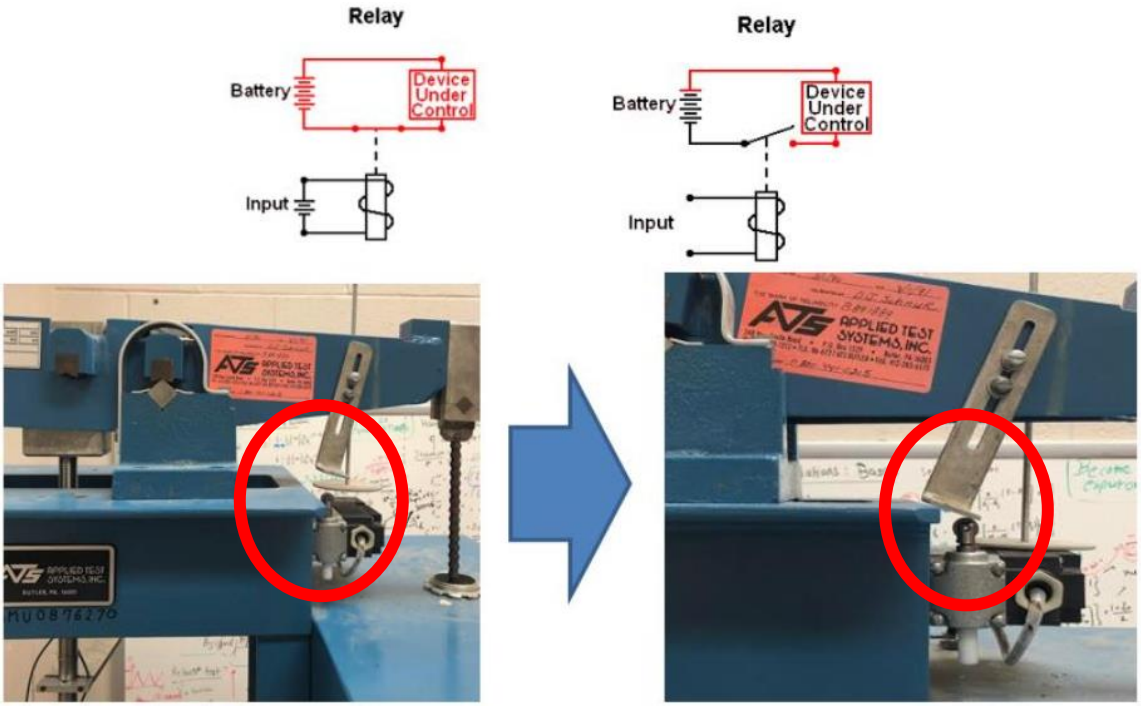

Figure 10. Contact switch for detecting sample fracture

In order to ensure the cooling and the surrounding temperature of the system, flow and thermostat switch were installed using the same relay mechanisms. Flow switch was installed at the outlet of the chiller, and it is to ensure the water flow inside the cooling pipes during the furnace operation. This switch is wired in a way that the furnace can only operate when there is at least 5 gpm of water flow detected at the outlet of the chiller.

Ensuring the flow during the creep test was not enough to ensure the safe operational temperature as it is possible that the compressor in the chiller malfunctions while there is still a flow detected in the flow switch. For such cases, a thermostat switch was attached to the surface of the furnace. This switch is wired in a way that the furnace will power off when the temperature of the surface exceeds 70 °C.

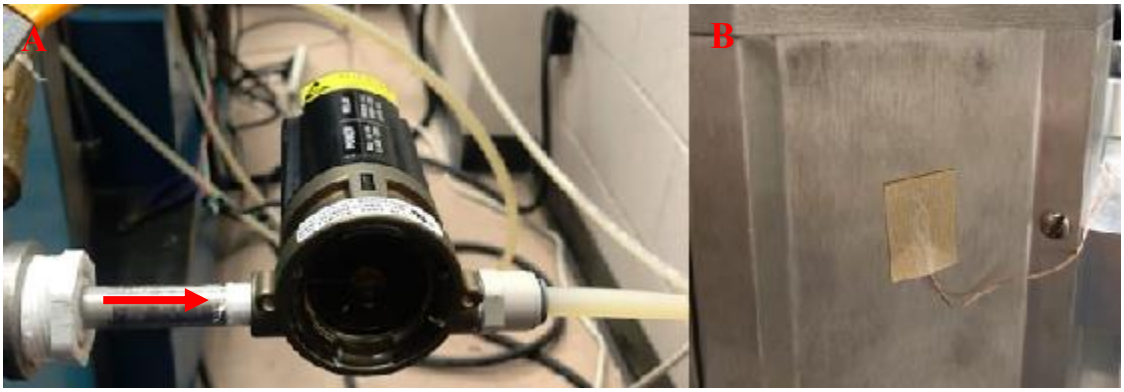

Figure 11. A) Flow switch B) thermostat switch

2.2. Sample Preparation

To study the triaxiality effect during creep, samples with notches were machined following Bridgman's equation which relates the notch radius to the triaxiality ratio: $T = \frac{1}{3} + \ln(1 + \frac{a}{2R})$. T is the triaxiality factor, a is the minimum cross section radius, and R is the notch radius. Triaxiality factors to be studied can be found in Table 1 and the samples that are accordingly machined are shown in Figure 12.


Figure 12. Machined samples with notches according to Bridgman's equation

Table 1. Triaxiality Campaign

T	Minimum Radius [mm]	Notch Radius [mm]
Uniaxial	1	
0.5	1	2.76
0.84	1	0.76
1	1	0.53

2.3. Creep Test

To check if the designed system was capable of performing creep tests, a uniaxial sample was tested at an already known condition, viz. 1050°C/230 MPa. Figure 13 shows the creep test result. The creep life was measured to be less than an hour, which was significantly different from the expected creep life that was found to be approximately 11 hours according to the Larson-Miller plot [22].

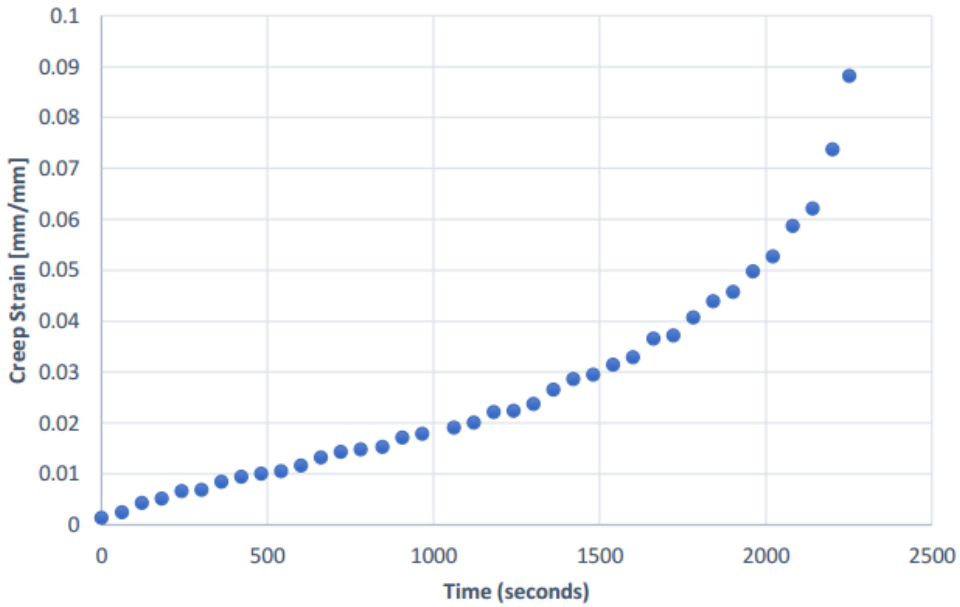

Figure 13. Uniaxial isothermal creep test at 230 MPa/1050°C

2.4. Scanning Electron Microscope Analysis

A sample of as received René N5 was prepared for SEM analysis by etching with 10 mL of hydrogen peroxide, 20 mL of hydrochloric acid, and 40 mL of distilled water in order to reveal the γ/γ' microstructure. Figure 14 shows the SEM image with the mean cube edge to be approximately 0.42 μm that was measured by image analysis. This value is not very different from the required mean cube edge for the highest creep resistance of the material, 0.45 μm [23]. The result indicates that this is not the reason for the significant discrepancy between the reported creep life and what was found during the experiment.

The problem was in fact with the γ/γ' eutectics that had not been properly eliminated. Figure 15 shows SEM images of other regions of the same sample where a) shows carbides that are inevitable during the solidification process. Carbides are known to have negligible effects on the creep life [23], but it is the eutectic that significantly affects the mechanical behavior of the superalloys. Eutectics are formed due to the refractory elements. As these elements diffuse slowly compared to other alloying elements, they form eutectics at the interdendritic regions during solidification process, which creates inhomogeneity within the material. As explained earlier, what makes the Ni-based single crystal superalloy strong is the homogenous γ' precipitates embedded in γ matrix throughout the material, and such inhomogeneity makes damage evolve faster. It is believed that this is the reason that made the experiment result different from the reported values. The material needs to be properly heat treated again to proceed.

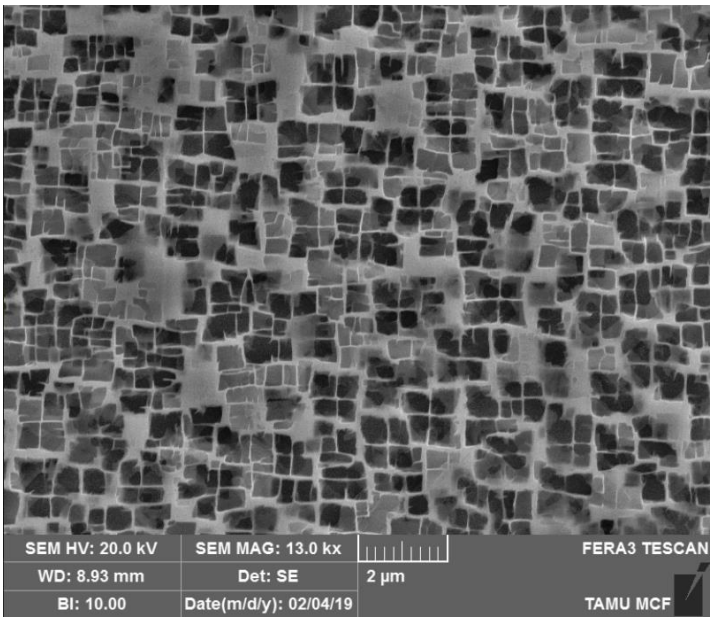

Figure 14. SEM image showing the γ and γ' phases

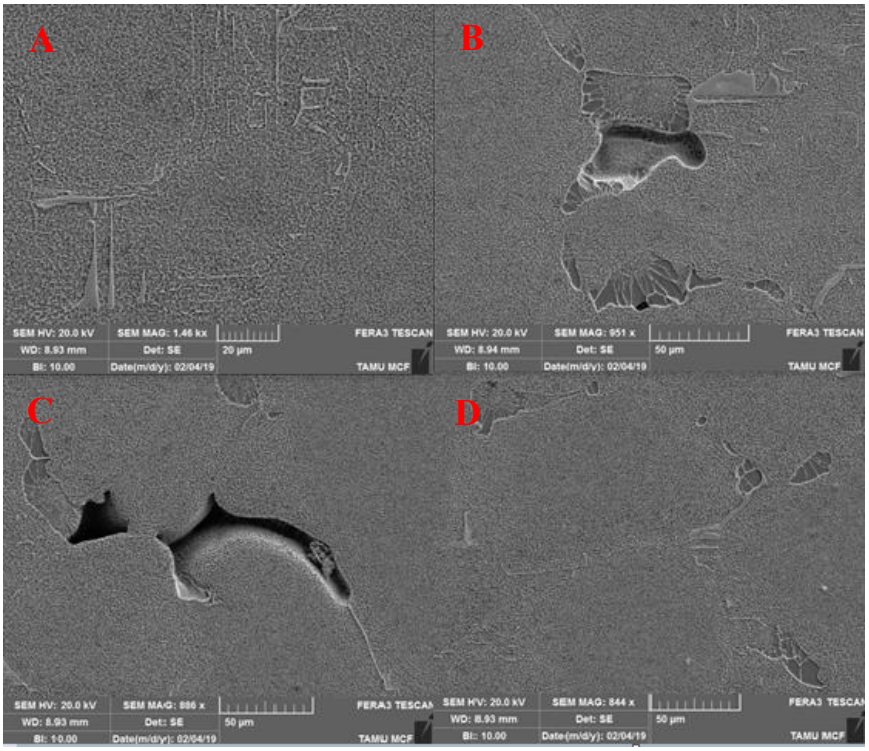

Figure 15. SEM images showing A) carbides, B) and C) euitectics attached to pores, D) eutectics

2.5. Thermogravimetric Test

In order to measure the kinetics of oxidation of René N5, samples of 1 mm in diameter and 6 mm in length cylinder were studied with Labsys Evo from Setaram.Inc., which is capable of performing thermogravimetric tests at temperatures up to 1200°C. The mass scale can be as accurate as a hundredth milligram upon proper calibration, and the heating rate was set at 2°C per minute. Two samples of identical size were tested at 1000°C for 100 hours. Figure 16 shows the result after taking out the non-isothermal part of the experiment. According to Georgia, et al., René N5 shows a mass increment of 0.2 mg/cm^2 whereas Bensch, et al. shows 0.3 mg/cm^2 at this condition [24, 25]. Both of the reported values are different from the experiment result which was found to be approximately 0.7 mg/cm^2. The discrepancies between the result and the literature may be due to size effect or different inlet airflow during the experiment.

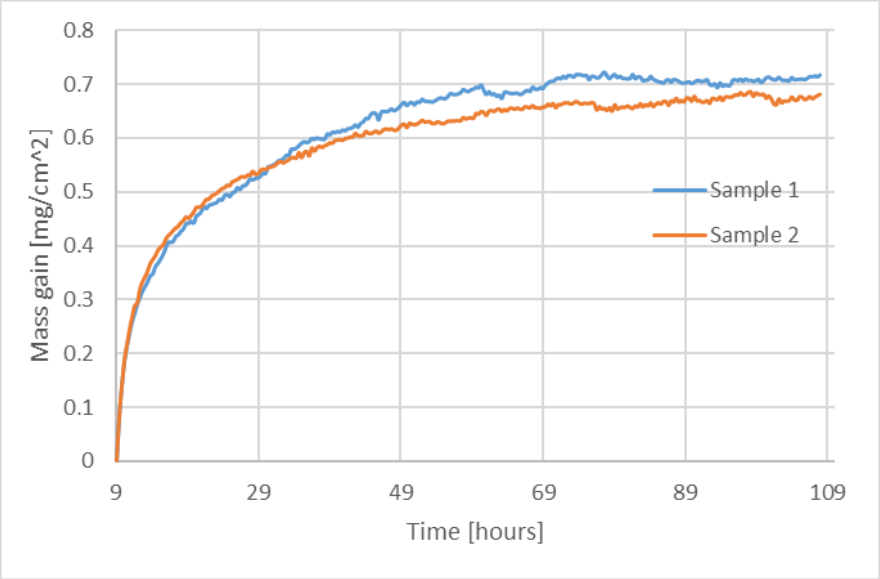

Figure 16. Isothermal part of thermogravimetric tests at 1000°C

3. MODELING[1]

3.1. Crystal plasticity framework

Eq. (1) shown below explains how the crystal plasticity framework works under the small strain assumption. The viscoplastic shear rate $\dot{\gamma}^s$ on a given slip system *s* in Eq. (2) is determined by means of the resolved shear stress τ^s, kinematic hardening x^s, isotropic hardening r^s. *K* and *n* that are temperature dependent material parameters. The resolved shear stress τ^s in Eq. (3) is calculated by knowing the applied stress tensor $\underline{\underline{\sigma}}$ and the orientation tensor $\underline{\underline{m}}^s$ which is calculated according to Eq. (4), where $\underline{n}^s$ and $\underline{l}^s$ are the normal to the slip system plane and the slip direction, respectively.

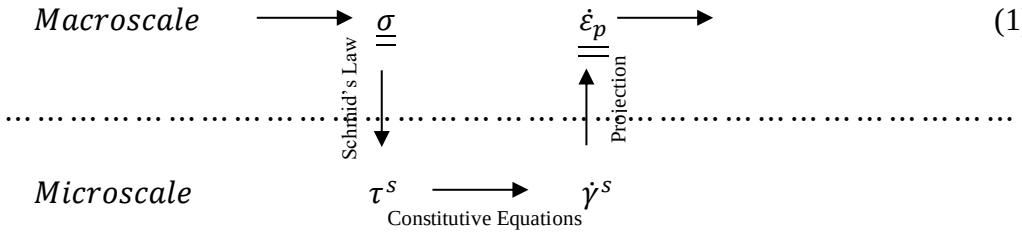

(1)

$$\dot{\gamma}^s = <\frac{|\tau^s - x^s| - r^s}{K}>^n sign(\tau^s - x^s) \quad (2)$$

$$\tau^s = \underline{\underline{\sigma}} : \underline{\underline{m}}^s \quad (3)$$

$$\underline{\underline{m}}^s = \frac{1}{2}(\underline{n}^s \otimes \underline{l}^s + \underline{l}^s \otimes \underline{n}^s) \quad (4)$$

[1]Part of this chapter is reprinted from "A microstructure-sensitive constitutive modeling of the inelastic behavior of single crystal nickel-based superalloys at very high temperature" by le Graverend, J.B., et al., 2014. Materials & Design 56, 990-997, Copyright 2013 by Elsevier.

Another important note in this model is that it only considers slip activities in octahedral slip systems ({111}<011> type). It is known that the cubic slip systems ({001} <011> type) are usually considered to model the mechanical behavior of samples with orientation away from <001>, such as <111> [7]. However, cubic slips are the results of the zig-zag motion of dislocations between adjacent octahedral slip systems at the microscales. Such movements can be modeled by additional octahedral slip systems [26, 27], but are not necessary here since cubic slip systems are not activated for <001> samples (Schmid factor equal to 0).

3.2. Isotropic and kinematic hardening

The isotropic hardening, which models the expansion of the yield curve, explicitly accounts for microstructural changes such as γ' coarsening that is either isotropic or directional. Isotropic hardening r^s in Eq. (5) depends on the dislocation density on each slip system, ρ^s that has a non-linear saturating form to account for the transition between the primary and secondary creep stage and the initial critical shear stress on each slip system, τ_0^s. The material parameters b, Q, G and B in Eq. (5) correspond to the kinetics of isotropic hardening that are related to the increase of dislocation density, the amplitude of isotropic hardening with an increase in dislocation density, the shear modulus, and the Burgers vector magnitude, respectively. The interaction matrix between slip systems [h], which appears in the second term of Eq. (5), was assumed to be the identity for sake of simplicity as the interaction matrix for complex alloys are not known, contrary to some pure metals like copper [28-30]. The third term is the *Orowan* stress that has been added

to account for the structural hardening/softening led by the γ' phase evolutions. The width of γ channel along the [001] direction, w_{001}, depends on the evolution of γ' volume fraction, and the $\sqrt{2/3}$ factor appeared for the calculation of *Orowan* stress as only octahedral slip systems are considered in the model.

$$r^s = \tau_0^s + bQ \sum_j h_{sj} \rho^j + \sqrt{\frac{2}{3}} \frac{GB}{w_{001}} \quad (5)$$

$$\dot{\rho}^s = (1 - b\rho^s)\dot{\gamma}^s \quad (6)$$

In order to capture the microstructural evolutions due to temperature changes, Eq. (7) proposes a new form of the non-linear kinematic hardening on each slip system s, x^s. The kinematic hardening, which is equivalent to a shift of the yield curve, is described by α^s which evolves non-linearly with the plastic slip γ^s, as shown in Eq. (8). The amount of internal stress that depends both on r^s and x^s is introduced in the material parameter *C* that was replaced by a parameter C^* depending on the temperature variation $\dot{T}$ through the variable a^*, as shown in Eq. (9) and (10). The scope of the proposed research is isothermal. Thus, the parameter C^* will be equal to *C* since a^* will always be equal to 1. The accumulated viscoplastic strain rate $\dot{p}$ is calculated according to Eq. (11) using the macroscopic viscoplastic strain rate tensor $\underline{\underline{\dot{\varepsilon}_p}}$.

$$x^s = C^* \alpha^s \quad (7)$$

$$\dot{\alpha}^s = (sign(\tau^s - x^s) - D^* \alpha^s) \times \dot{\gamma}^s \quad (8)$$

$$C^* = a^* C \tag{9}$$

$$\dot{a}^* = \frac{a^* \dot{T}}{\alpha^*} - \frac{(a^* - 1)}{\beta^*} \text{ where } a^*(t = 0) = 1 \tag{10}$$

$$\dot{p} = \sqrt{\frac{2}{3} \underline{\underline{\dot{\varepsilon}_p}} : \underline{\underline{\dot{\varepsilon}_p}}} \; where \; \underline{\underline{\dot{\varepsilon}_p}} = \sum_s \dot{\gamma}^s \underline{\underline{m}}^s \tag{11}$$

Non-isothermal conditions above 950 °C lead to the release of γ/γ' interfacial dislocations and this phenomenon is captured by the first term in Eq. (10). It was observed that a temperature spike re-establishes the dislocation structure during *in situ* non-isothermal creep tests under X-ray synchrotron radiation [31], which is accounted by the second term. Both α^* and β^* are the time constants.

$$D^* = D\left(1 + \frac{f_s}{f_l} K_f\right) \tag{12}$$

$$\dot{f}_l = \left[1 - \delta_l \times \exp\left(-\frac{p}{e_{cfl}}\right)\right] \frac{(f_{eq} - f_l)}{\alpha_l} \tag{13}$$

$$if \; \left(f_{eq} - f_l\right) \leq 0 \; then \; \dot{f}_s = -\frac{f_s}{\alpha_s} \tag{14}$$

$$if \; \left[\left(f_{eq} - f_l\right) > 0 \; and \; \dot{T} < 0\right] \; then \; \dot{f}_s = -\frac{f_{eq} - f_l - f_s}{\alpha_s} \frac{\dot{T}}{\dot{T}_0} - \left(\frac{f_s}{K_{s1}}\right)^{m_s} \tag{15}$$

$$if \; \left[\left(f_{eq} - f_l\right) > 0 \; and \; \dot{T} \geq 0\right] \text{ then } \dot{f}_s = -\left(\frac{f_s}{K_{s2}}\right)^{m_s} \tag{16}$$

The expression D^* in Eq. (12) modifies the kinetics of the kinematic hardening. The asymptotic value of the kinematic hardening is $\pm C/D$, which was established from cyclic tests [7]. D is a temperature-dependent material parameter and K_f is a material

parameter which expresses the effect of γ' precipitate evolution on the kinetics of the kinematic hardening. Parameters α_s and α_l are time constants for the evolutions of small and large γ' precipitate volume fractions f_s and f_l, respectively. e_{cfl} is the creep strain that accounts for the dislocation density saturation in the matrix. $\dot{T}_0$ in Eq. (15) is a constant rate of change in temperature, f_{eq} is the γ' volume fraction at the equilibrium state, and lastly K_{s1}, K_{s2}, m_s, and δ_l are all temperature-dependent material parameters.

3.3. Microstructural evolutions of the γ' precipitates

Thermal loading at temperature above 950°C leads to dissolution/precipitation of the γ' precipitates that affects the γ channel width w_{001}. This can be related to the evolution of the large and small precipitate volume fractions [32], and this relation has been validated by non-isothermal synchrotron tests [31]. The function $f_{thermic}$ in Eq. (17) gives the contribution of the thermal loading to w_{001} evolution. *ml*, d_{tp} and *msp* are temperature-independent material parameters. The γ channel width w_{001}'s dependence on f_l was studied using image analysis [32].

$$f_{thermic} = f_l^{ml} - d_{tp} \times f_s^{msp} \tag{17}$$

$$\dot{f}_{isotropic} = \frac{f_{isotropic}^3(t_0)\chi_0 \exp(\frac{-U_t}{RT})}{3f_{isotropic}^2} \tag{18}$$

The function $f_{isotropic}$ in Eq. (18) represents the contribution of thermal holding, or aging, to w_{001} evolution. In fact, high temperature condition leads to homothetic growth

of γ' precipitates, which eventually causes spheroidization and an isotropic coarsening of γ' precipitates. The driving force for such phenomenon is the reduction of the internal γ/ γ' interfacial energy. This makes the $f_{isotropic}$ only dependent on time and temperature and independent of deformation/stress state. In this equation, T, U_t, R and χ_0 are the temperature in Kelvin, the activation energy (in $Jmol^{-1}$), the gas constant (8.314 $Jmol^{-1}K^{-1}$) and non-temperature dependent model parameter, respectively. Lifschitz-Slyosov-Walter (LSW) theory suggests that the particles coarsening controlled by diffusion is cube root dependent with time when the precipitate volume fraction is small [33, 34]. Although this theory does not seem to apply for single crystal superalloys as the theory itself was developed for binary system and for spherical particles, Ardell has shown that the assumption for a diffusion controlled growth may remain valid in Ni-based single crystal superalloys [35].

Depending on the sign, the stress state as well as the misfit of the single crystal superalloys affect the direction of the coarsening of γ' precipitates due to in the internal stress distribution. When a certain value of dislocation density is reached, the γ' rafting process occurs [36]. This provides a motivation to develop a set of constitutive equations to consider the dependence of γ' rafting process into accumulated viscoplastic strain p. The function $f_{mechanic}$ in Eq. (19), which represents the contribution of mechanical loadings to w_{001} evolution, takes viscoplastic strain as its main component and makes the rafting process possible at high temperature even without any external load as long as a given viscoplastic strain is reached, as observed by Reed [37]. Thus, the function $f_{mechanic}$ also depends on the function $f_{diffusion}$ that shows the effect of diffusion on the

microstructural evolution, and the new internal variable ξ which accounts for a strain rate effect as shown in Eq. (20) and Eq. (21), respectively.

$$f_{mechanic} = \frac{f_{diffusion}\sqrt[3]{p}}{1+sinh^{-1}(\xi \times \nu_0)} \tag{19}$$

$$\dot{f}_{diffusion} = \frac{1}{\tau_{diffusion}}\left(K_0 - f_{diffusion}\right) \tag{20}$$

$$\dot{\xi} = \left(\frac{\dot{\nu}^2}{\xi_0} - \xi\right) \times \dot{\nu} - \left(\frac{\xi}{M}\right)^m \tag{21}$$

$$\tau_{diffusion} = \frac{d^2}{2D_{Al}^{\gamma'}(T)} \tag{22}$$

In the equations above, M, m, ξ_0, ν_0 and K_0 are model parameters that are temperature dependent. In Eq. (21), the first term gives smooth evolutions of $f_{mechanic}$ for short and highly deformed tests, which increases the value of ξ. This will decrease the $f_{mechanic}$, which also means less γ' rafting process developed. The second term gives a recovery effect for tests having several plastic strain rates. Eq. (22) represents the characteristic time of diffusion. It was observed that the diffusion of γ' elements in the γ' phase limits the γ' rafting rate [37], thus the diffusion of aluminum in the γ' phase was chosen to be considered in the equation. $D_{Al}^{\gamma'}$ is the diffusion coefficient of aluminum in the γ' phase and d is the mean free path for diffusion [14].

All these contributions come to an expression of the w_{001} show as Eq. (23).

$$w_{001} = w_0 \times f_{thermic} \times (1 + f_{mechanic} + f_{isotropic}) \quad (23)$$

3.4. Damage evolution due to oxidation

In order to consider the effect of oxidation, it is important to know the kinetics of oxide scale growth. Hou and Chou [38] confirmed that increments of both the mass gain and the thickness of oxide layer follow a diffusion law for oxidation behavior. Furthermore, Sato at al. were also successful in describing the evolution of the oxide scale thickness following the parabolic law of oxidation behavior in thin-walled specimens of René N5 at 1000°C [39]. Both cases accounted for the variation of the oxidation constant depending on the oxidation stages [17]. The oxidation behavior of most of alloys, however, is known to be linear, parabolic, logarithmic, or often combination of the three when the oxidation constant is assumed to be constant with time [40]. For the simplicity of the modeling process, the oxidation constant will be assumed to be constant with time, and the logarithmic oxidation behavior will be assumed, as this behavior has been observed in many thermogravimetric tests for Ni-based single crystal superalloys [17, 18, 24]. The kinetics of the oxide scale growth is proposed in Eq. (24). C_n is a temperature dependent material parameter and K_{ox} is the oxidation constant.

As discussed in the Introduction, the initial surface roughness affects the kinetics of oxidation. It is believed that there is a critical value of initial surface roughness that favors the oxidation the most and a deviation from this value will decrease the oxidation rate. In order to describe such phenomenon, a modified Gaussian function, so called gamma distribution function, has been used, as shown in Eq. (25), to describe the surface

roughness effect on the oxide scale growth. Ra is the average initial surface roughness, and μ, β, as well as γ are the function parameters that determine the shape, scale, and the location of the gamma distribution function, respectively. Eq. (27) calculates A_{ox} with e_{ox} in Eq. (24) and a temperature dependent material parameter A, which modifies the damage kinetics $\dot{D}_c$ in Eq. (29).

$$\dot{e}_{ox} = C_n K_{ox} \exp\left(-\frac{e_{ox}}{C_n K_{ox}}\left(1+\sqrt{p}\right)\right) * f(Ra) \tag{24}$$

$$f(Ra) = \frac{\left(\frac{Ra-\mu}{\beta}\right)^{\gamma-1} exp(-\frac{Ra-\mu}{\beta})}{\beta\Gamma(\gamma)} \tag{25}$$

$$\Gamma(\gamma) = \int_0^\infty t^{\gamma-1} e^{-t} dt \tag{26}$$

$$A_{ox} = A/(1+e_{ox}) \tag{27}$$

3.5. Damage evolution due to the multiaxiality

Having the multiaxial stress state means the applied stress tensor $\underline{\sigma}$ must be modified to account for the damage due to the multiaxiality. Eq. (28) shows the effective stress tensor, and the damage density function in Eq. (29) has a Rabotnov-Kachanov law type formulation [41]. D_C depends on the Hayhurst's stress [42] and the parameters α and β in the Hayhurst's stress $\chi(\underline{\sigma})$ were given by Lesne for single crystal superalloys [42]. In the Eq. (28), $J_0\left(\underline{\sigma}\right)$ represents the maximum principal stress, $J_1\left(\underline{\sigma}\right)$ is equivalent

to the trace of the applied stress tensor, $J_2\left(\underline{\underline{\sigma}}\right)$ is the von Mises stress with r and k being temperature-dependent material parameters.

$$\underline{\underline{\sigma}}_{eff} = \frac{\underline{\underline{\sigma}}}{1-D_c} \tag{28}$$

$$\dot{D}_c = \left(\frac{\chi\left(\underline{\underline{\sigma}}\right)}{A_{ox}}\right)^r (1-D_c)^{-k} \tag{29}$$

$$with\ \chi(\underline{\underline{\sigma}}) = \alpha J_0\left(\underline{\underline{\sigma}}\right) + \beta J_1\left(\underline{\underline{\sigma}}\right) + (1-\alpha-\beta)J_2\left(\underline{\underline{\sigma}}\right)$$

4. SIMULATION

4.1. Evolution of e_{ox} over Time

As discussed previously, logarithmic behavior was assumed for the oxide scale growth. The simulation results with different plasticity values are shown in Figure 17 where the corresponding plasticity values, pl0 to pl4, were generated by simulating a general creep curve shown in Figure 18. The specific values can be found in Table 2. The model was able to show the trend where the increase of plasticity increases the kinetics of oxide scale growth.

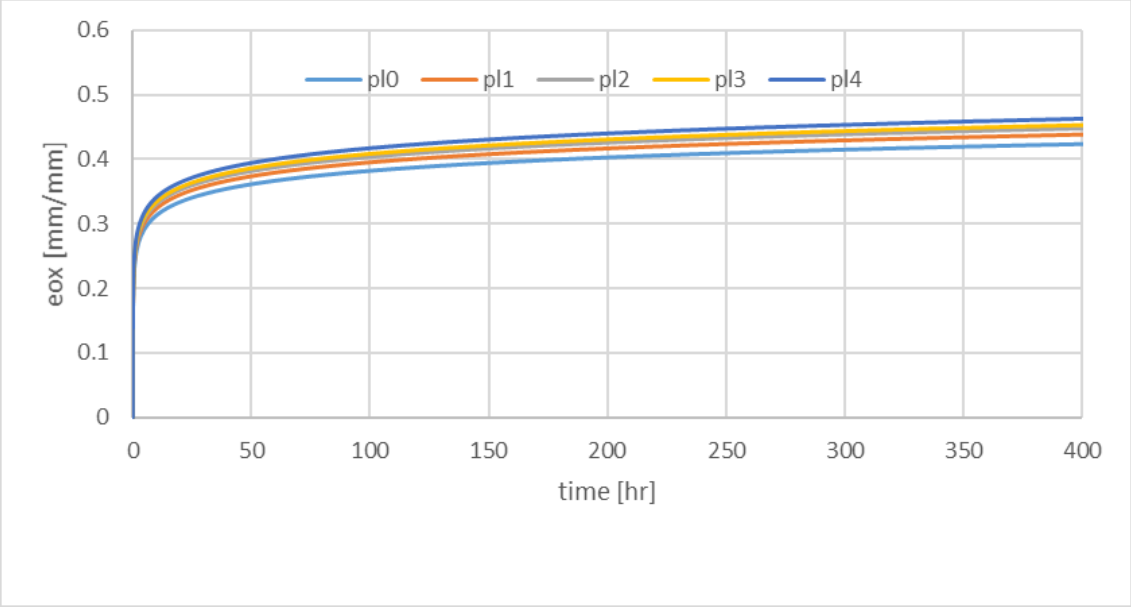

Figure 17. Simulation result of e_{ox} evolution at 1050°C with different initial plastic strain

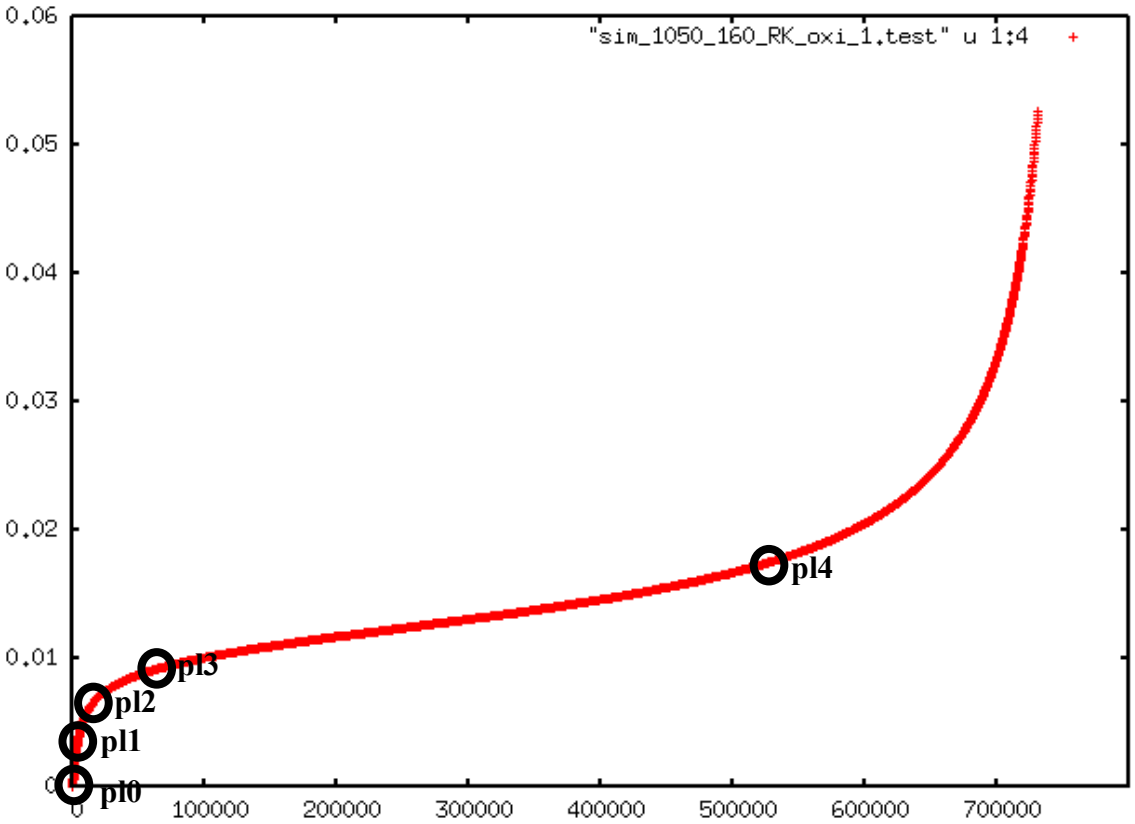

Figure 18. Creep curve with corresponding plasticity values used in Figure 17

Table 2. Plasticity values used in the simulation

Accumulated Plastic Strain	Strain %
pl0	0
pl1	0.05
pl2	0.1
pl3	0.18
pl4	0.34

Figure 19 shows the simulation result of the evolution of e_{ox} for different surface roughness. The modeling parameters for the gamma distribution function, which carries the effect of the surface roughness on the e_{ox} evolution, are tabulated in Table 3. The model successfully described the trend where finer surface roughness results into higher oxidation kinetics. The e_{ox} curve for Ra = 0.09 µm shows higher oxidation kinetics than the curve for Ra = 0.019 µm, which implies that the observed trend that there is a critical surface roughness value that favors the oxidation the most has been successfully modeled, as well. However, the difference between the curves are not as distinct as what is found in the thermogravimetric test results from Pei, et al. It is still necessary to modify the $f(Ra)$ to represent the phenomenon better.

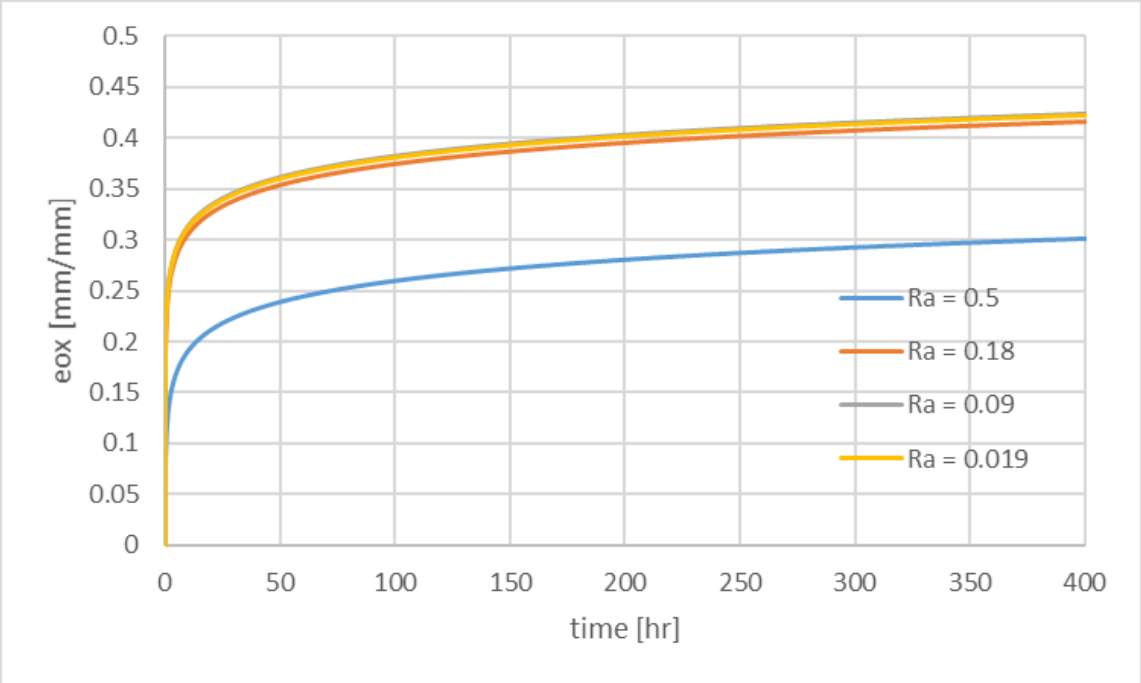

Figure 19. Simulation result of e_{ox} evolution at 1050 °C with different surface roughness

Table 3. Gamma Distribution Function Parameters

Purpose	Parameters	Values
Location	μ	0.017
Shape	γ	1.3
Scale	β	0.08

4.2. 2D and 3D simulation of creep in both air and in vacuum

Figure 20 shows the simulation results of creep curves with and without oxidation. It is clear that the creep curve with oxidation has higher minimum creep rate and earlier fracture time than the creep curve without oxidation. Although there is no data available for direct comparison in the literature, there are some other reported experiment results that tested similar metallic materials and compared air and vacuum. Bueno et al. performed creep tests on 2.25Cr-1Mo steel both in air and in vacuum condition at 700°C/525 MPa, and the air case resulted in higher minimum creep rate and earlier fracture time [43]. Dryepondt et al. also pointed out similar trends through performing creep tests on Ni-based single crystal superalloy MC2 both in air and in hydrogenated argon [15].

Finite element simulation was performed to visualize how the modification of the previous model affects the simulation results. Figure 21 shows the boundary conditions and the specimen geometry employed to perform the simulation on MC2 alloy at 1050°C/138 MPa that is equivalent to the one used in le Graverend, et al. [7]. Simulation result of the evolution of the accumulated plastic strain in air is drawn in Figure 22, in which the values are found to be relatively high in the notched area due to high triaxiality

factor. Figure 23 shows the evolution of e_{ox} that evolves faster near the notched area where the accumulated plastic strain is high. The model without oxidation showed the lifetime of 16.7 hours whereas it showed 9.3 hours with oxidation.

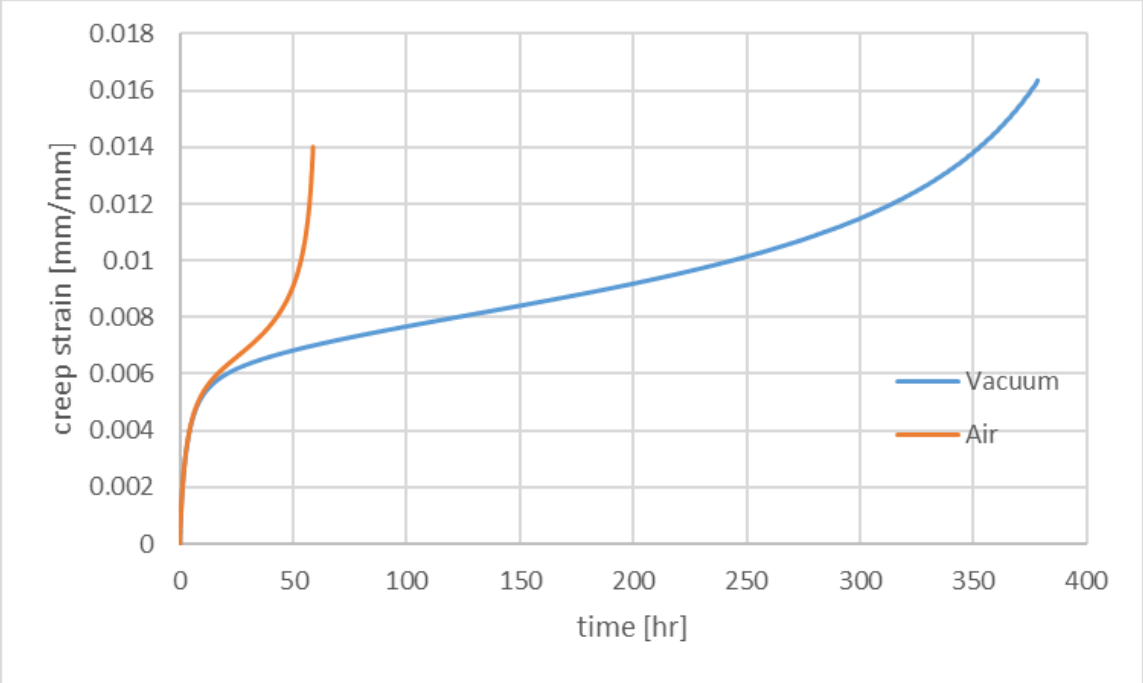

Figure 20. Simulated creep curves both in air and in vacuum

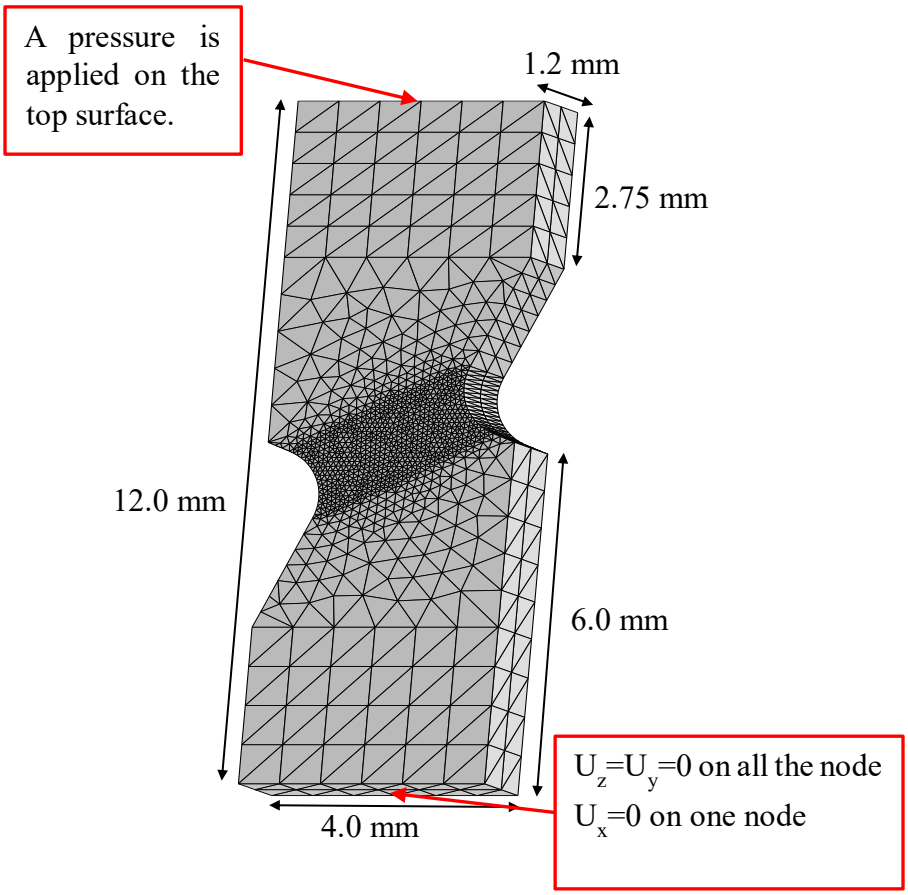

Figure 21. Finite element simulation mesh, condition, and geometry

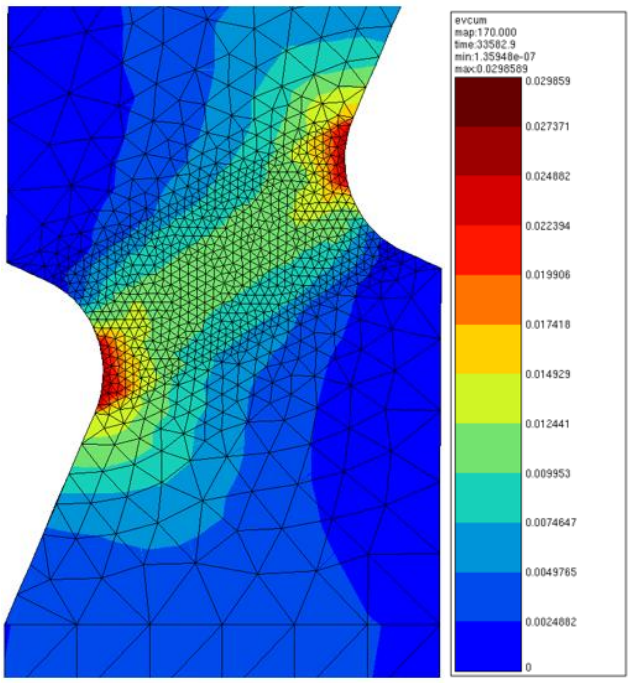

Figure 22. Evolution of the accumulated plastic strain in air

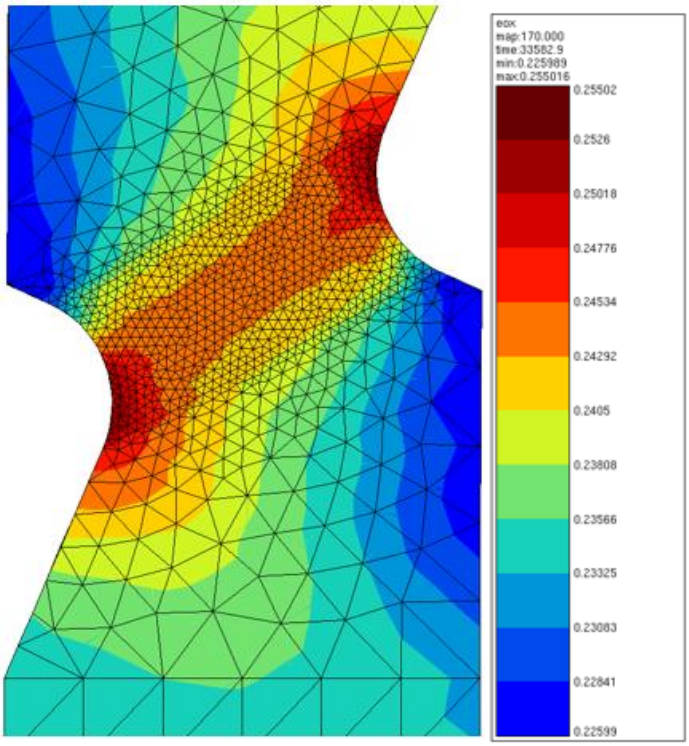

Figure 23. e_{ox} evolution

5. CONCLUSIONS

5.1. Conclusion

Oxidation affects the microstructural stability of Ni-based single crystal superalloys through depletion of the γ' precipitates, which decreases the load-bearing capacity. As the strength of the superalloys is based on the volume fraction of the γ' precipitates, this gives a fundamental motivation to study the oxidation kinetics. Two factors that affect the oxide scale growth have been studied.

The oxide scale growth increases with a decrease in the surface roughness, or finer surface. However, there is a critical surface roughness that favors the oxidation the most, and this phenomenon was well described in a function that carries the surface roughness effect on oxidation. The oxide scale growth also increases with plastic strain. This phenomenon was well explained with the concept of pipe line diffusion and Cottrell atmosphere. A dimensionless variable e_{ox} was introduced to represent the depleted zone thickness and it was well implemented in the model to show adequate variation of e_{ox} evolution for various plasticity and surface roughness values.

Although it was not possible to compare the simulation results directly with the experimental data, the simulation results showed the same trends that were found in other similar metallic materials. This implies that the model is conceptually working.

5.2. Future work

The original plan of the research includes performing multiaxial creep experiments. However, the given René N5 was found to show too many eutectic regions that had not been properly eliminated. This superalloy needs to be heat treated again but the heat treatment facility was not available during the period of research. This is the reason that the lattice rotation due to multiaxiality has not been discussed. Figure 3 shows the EBSD analysis which shows that the lattice rotation occurred near the notched area, or areas with high triaxiality. When the material is heat treated properly, a further study needs to be performed on the lattice rotation by performing multiaxial creep experiments following the proposed campaign shown in Table 1.

If the orientation of the specimen changes, the direction of the slip plane and slip direction changes, which will modify the mechanical response. This suggests the modification in the orientation tensor $\underline{\underline{m}}^s$ that accounts for the normal to the slip plane and slip direction. The effective orientation tensor $\underline{\underline{m}}^s_{eff}$ can be calculated according to Eq. (30) where $\underline{\underline{m}}^s$ is the initial orientation tensor and $\underline{\underline{R}}$ is the lattice rotation tensor which follows the work of Lebensohn and Tomé [44] shown in Eq. (31). The first term $\dot{\Omega}_{ij}$ represents the antisymmetric component of the macroscopic distortion rate and the rest is that of the plastic distortion rate. The modification of the orientation tensor also modifies the value of the resolved shear stress τ^s to the effective resolved shear stress τ^s_{eff}, according to Eq. (32).

$$\underline{\underline{m}}^{s}_{eff} = \underline{\underline{R}}\,\underline{\underline{m}}^{s}\,\underline{\underline{R}}^{T} = \underline{\underline{R}}[\tfrac{1}{2}\left(\underline{n}^{s}\otimes\underline{l}^{s} + \underline{l}^{s}\otimes\underline{n}^{s}\right)]\underline{\underline{R}}^{T} \quad (30)$$

$$\dot{R}_{ij} = \dot{\Omega}_{ij} - \sum_{s}\left(l_i n_j - l_j n_i\right)^{s}\dot{\gamma}^{s} \quad (31)$$

$$\tau^{s}_{eff} = \underline{\underline{\sigma}}_{eff} : \underline{\underline{m}}^{s}_{eff} \quad (32)$$

REFERENCES

1. Caron, J.L. and J.W. Sowards, *6.09 - Weldability of Nickel-Base Alloys*, in *Comprehensive Materials Processing*, S. Hashmi, et al., Editors. 2014, Elsevier: Oxford. p. 151-179.

2. Geddes, B., H. Leon, and X. Huang, *Superalloys: alloying and performance*. 2010, Ohio: ASM International.

3. Betteridge, W. and S.W.K. Shaw, *Development of superalloys.* Materials Science and Technology, 1987. **3**(9): p. 682-694.

4. Carry, C. and J.L. Strudel, *Apparent and effective creep parameters in single crystals of a nickel base superalloy—II. Secondary creep.* Acta Metallurgica et Materialia, 1978. **26**(5): p. 859-870.

5. Pollock, T.M. and A.S. Argon, *Creep resistance of CMSX-3 nickel base superalloy single crystals.* Acta Metallurgica et Materialia, 1992. **40**(1): p. 1-30.

6. Vattré, A., *Strength of single crystal superalloys: from dislocation mechanisms to continuum micromechanics.* PhD These, 2009(ONERA The French Aerospace Lab): p. 155.

7. Le Graverend, J.-B., et al., *A microstructure-sensitive constitutive modeling of the inelastic behavior of single crystal nickel-based superalloys at very high temperature.* International Journal of Plasticity, 2014. **59**: p. 55-83.

8. Argon, A. and W.C. Moffatt, *Climb of extended edge dislocations.* Acta Metallurgica et Materialia, 1981. **29**: p. 293-299.

9. le Graverend, J.B., et al., *Effect of fine γ′ precipitation on non-isothermal creep and creep-fatigue behaviour of nickel base superalloy MC2*. Materials Science and Engineering: A, 2010. **527**(20): p. 5295-5302.

10. le Graverend, J.B., et al., *Highly non-linear creep life induced by a short close γ′-solvus overheating and a prior microstructure degradation on a nickel-based single crystal superalloy.* Materials & Design (1980-2015), 2014. **56**: p. 990-997.

11. Ignat, M., J.-Y. Buffiere, and J.M. Chaix, *Microstructures induced by a stress gradient in a nickel-based superalloy.* Acta metallurgica et materialia, 1993. **41**(3): p. 855-862.

12. Ardakani, M.G., M. McLean, and B.A. Shollock, *Twin formation during creep in single crystals of nickel-based superalloys.* Acta materialia, 1999. **47**(9): p. 2593-2602.

13. Ghosh, R., R. Curtis, and M. McLean, *Creep deformation of single crystal superalloys—modelling the crystallographic anisotropy.* Acta Metallurgica et Materialia, 1990. **38**(10): p. 1977-1992.

14. Le Graverend, J.B., et al., *Dissolution of fine γ'precipitates of MC2 Ni-based single-crystal superalloy in creep-fatigue regime.* Advanced Materials Research, 2011. **278**: p. 31-36.

15. Dryepondt, S., et al., *Static and dynamic aspects of coupling between creep behavior and oxidation on MC2 single crystal superalloy at 1150 °C.* Acta Materialia, 2005. **53**(15): p. 4199-4209.

16. Charpentier, L., et al., *Influence of surface roughness and temperature on the oxidation behavior of ZrC/SiC samples.* Ceramics International, 2016. **42**(9): p. 10985-10991.

17. Pei, H., et al., *Influence of surface roughness on the oxidation behavior of a Ni-4.0Cr-5.7Al single crystal superalloy.* Applied Surface Science, 2018. **440**.

18. Reuchet, J. and L. Remy, *Fatigue oxidation interaction in a superalloy—application to life prediction in high temperature low cycle fatigue.* Metallurgical Transactions A, 1983. **14**(1): p. 141-149.

19. Dubey, V., S. Roychowdhury, and V. Kain, *Effect of cold working on oxidation behavior and nature of oxide film formed on carbon steel.* Materials and Corrosion, 2018. **69**(7): p. 908-916.

20. Höfler, D.-I.-P.A., *Tensile Test*, in *TEC-Science*.

21. *Instruction Manual E4 Chamber Heater.* Research Inc.: p. 8.

22. Wahl, J. and K. Harris, *New single crystal superalloys – overview and update*, in *EUROSUPERALLOYS 2014 – 2nd European Symposium on Superalloys and their Applications*, J.Y. Guedou, Editor. 2014, EDP Sciences. p. 17002.

23. Caron, P. and T. Khan, *Evolution of Ni-based superalloys for single crystal gas turbine blade applications.* Aerospace Science and Technology, 1999. **3**(8): p. 513-523.

24. Bensch, M., et al., *Modelling and analysis of the oxidation influence on creep behaviour of thin-walled structures of the single-crystal nickel-base superalloy Rene N5 at 980 deg C.* Acta Materialia, 2010. **58**(5): p. 1607-1617.

25. Georgia Obigodi-Ndjeng, M., *High Temperature Oxidation and Electrochemical Investigations on Ni-base Alloys.* PhD These, 2011(Universität Erlangen-Nürnberg(46043734)): p. 182.

26. Vattré, A., B. Devincre, and A. Roos, *Orientation dependence of plastic deformation in nickel-based single crystal superalloys: Discrete–continuous model simulations.* Acta Materialia, 2010. **58**(6): p. 1938-1951.

27. Vattré, A. and B. Fedelich, *On the relationship between anisotropic yield strength and internal stresses in single crystal superalloys.* Mechanics of Materials, 2011. **43**(12): p. 930-951.

28. Franciosi, P., *The concepts of latent hardening and strain hardening in metallic single crystals.* Acta Metallurgica, 1985. **33**(9): p. 1601-1612.

29. Gérard, C., G. Cailletaud, and B. Bacroix, *Modeling of latent hardening produced by complex loading paths in FCC alloys.* International Journal of Plasticity, 2013. **42**: p. 194-212.

30. Tabourot, L., M. Fivel, and E. Rauch, *Generalised constitutive laws for f.c.c. single crystals.* Materials Science and Engineering: A, 1997. **234-236**: p. 639-642.

31. Le Graverend, J.-B., et al., *In situ measurement of the γ/γ' lattice mismatch evolution of a nickel-based single-crystal superalloy during non-isothermal very high-temperature creep experiments.* Metallurgical and Materials Transactions A, 2012. **43**(11): p. 3946-3951.

32. Cormier, J. and G. Cailletaud, *Constitutive modeling of the creep behavior of single crystal superalloys under non-isothermal conditions inducing phase transformations.* Materials Science Engineering: A, 2010. **527**(23): p. 6300-6312.

33. Lifshitz, I.M. and V.V. Slyozov, *The kinetics of precipitation from supersaturated solid solutions.* Journal of Physics and Chemistry of Solids, 1961. **19**(1-2): p. 35-50.

34. Wagner, C., *Theorie der alterung von niederschlägen durch umlösen (Ostwald-reifung).* Zeitschrift für Elektrochemie, Berichte der Bunsengesellschaft für physikalische Chemie, 1961. **65**(7-8): p. 581-591.

35. Ardell, A. and R. Nicholson, *The coarsening of γ'in Ni-Al alloys.* Journal of Physics and Chemistry of Solids, 1966. **27**(11-12): p. 1793-1794.

36. Embury, J.D., A. Deschamps, and Y. Brechet, *The interaction of plasticity and diffusion controlled precipitation reactions.* Scripta Materialia, 2003. **49**(10): p. 927-932.

37. Reed, R., D. Cox, and M. Rae, *Kinetics of rafting in a single crystal superalloy: effects of residual microsegregation.* Materials Science and Technology, 2007. **23**(8): p. 893-902.

38. Hou, X.M. and K.C. Chou, *Quantitative interpretation of the parabolic and nonparabolic oxidation behavior of nitride ceramic.* Journal of the European Ceramic Society, 2009. **29**(3): p. 517-523.

39. Reed, R.C., *The superalloys: fundamentals and applications*. 2008, Cambridge: Cambridge university press.

40. Younes, C.M., G.C. Allen, and J.A. Nicholson, *High temperature oxidation behaviour of single crystal superalloys RR3000 and CMSX-4.* Corrosion Engineering, Science and Technology, 2007. **42**(1): p. 80-88.

41. Rabotnov, Y.N., *Creep problems in structural members.* Applied Mathematics and Mechanics Series, 1969. **7**.

42. Hayhurst, D.R., *Creep rupture under multi-axial states of stress.* Journal of the Mechanics and Physics of Solids, 1972. **20**(6): p. 381-382.

43. Bueno, L.d.O., V.L. Sordi, and L. Marino, *Constant load creep data in air and vacuum on 2.25Cr-1Mo steel from 600C to 700C* Materials Research, 2005. **8**: p. 401-408.

44. Lebensohn, R.A. and C. Tomé, *A self-consistent anisotropic approach for the simulation of plastic deformation and texture development of polycrystals: application to zirconium alloys.* Acta metallurgica et materialia, 1993. **41**(9): p. 2611-2624.